A parametric study on the final blade installation process for monopile wind turbines under rough environmental conditions

Zhiyu Jiang[a,b], Zhen Gao[a,b,c], Zhengru Ren[a,b,c], Ye Li[d,e,f,g,*], Lei Duan[d]

[a] *Department of Marine Technology, Norwegian University of Science and Technology (NTNU), NO-7491 Trondheim, Norway*
[b] *Centre for Research-based Innovation of Marine Operations (SFI MOVE), NTNU, NO-7491 Trondheim, Norway*
[c] *Centre for Autonomous Marine Operations and Systems (SFF AMOS), NTNU, NO-7491 Trondheim, Norway*
[d] *School of Naval Architecture, Ocean & Civil Engineering, Shanghai Jiao Tong University (SJTU), Shanghai 200240, China*
[e] *State Key Laboratory of Ocean Engineering, School of Naval Architecture, Ocean & Civil Engineering, SJTU, Shanghai 200240, China*
[f] *Collaborative Innovation Center for Advanced Ship and Deep-Sea Exploration, SJTU, Shanghai 200240, China*
[g] *Key Laboratory of Hydrodynamics (Ministry of Education), SJTU, Shanghai 200240, China*

Abstract

Single blade installation is a method for installing wind turbine blades. If a jack-up vessel is used during an offshore installation, the wind turbine blade is mainly subjected to wind loads and experiences resonant motions, and the monopile is subjected to wave-induced vibrations. The blade mating process can be challenging if large relative motions occur between the blade root and the monopile top. This study numerically models a blade installation system that consists of a pre-installed monopile and nacelle assembly, and a 5 MW blade with tugger lines. By analyzing the blade-root and the hub motion radii from time-domain simulations, we evaluate the effects of mean wind speed, wind turbulence, significant wave height, wave spectral peak period, wind-wave misalignment, and water depth on the blade installation. For the alignment phase, the blade-root motion is critical, especially when the mean wind speed and turbulence are high. The hub motion can be important when the monopile resonant responses are prominent. The relative in-plane motions rather than the hub or the blade motion alone should be considered during the assessment. For the mating phase, the high-frequency components of the responses are important in general. Because of the dominant flange-hole motions at the monopile top, an increase in water depth reduces the success rate of mating.

Keywords: single blade installation; alignment; mating; blade motion; monopile vibration; outcrossing rate; environmental condition

1. Introduction

Different methods exist for mounting blades on offshore wind turbines. Many offshore wind turbines are typically pre-assembled into a single rotor component before they are loaded onto a vessel. This method minimizes the number of offshore lifts and provides a relatively low-cost solution. However, with rotor diameters approaching 200 meters (m) for the largest announced wind turbines [1], the maneuvering and transport task of this installation technique is due for change.

*Corresponding author
Email addresses: zhiyu.jiang@ntnu.no (Zhiyu Jiang), zhen.gao@ntnu.no (Zhen Gao), zhengru.ren@ntnu.no (Zhengru Ren), ye.li@sjtu.edu.cn (Ye Li), lduansjtu@yeah.net (Lei Duan)

Single blade installation waves goodbye to the minimal lifts principle, but also to the practice of assembling rotors on land, instead delaying assembly until the installation vessel is on location. The installation is often performed with a yoke that seizes the blade by its mass center and lifts the blade by a crane to the hub position at the monopile top. Because of the limitations imposed by state-of-the-art lifting equipment, single blade installation is convenient up to wind speeds of approximately 8 to 12 m/s [2]. Thereby, considerable time and money have been spent waiting for low wind speed time windows during the construction of offshore wind farms.

To address this issue, researchers have undertaken efforts to better understand the aerodynamic and aeroelastic behaviors of the installation situations. Wang et al. [3] investigated the hoisting forces on a wind turbine blade using computational fluid dynamics (CFD) methods. Gaunaa et al. [2] proposed a first-order engineering model to describe the aerodynamic forcing on a blade using the cross-flow principle. The model was in good agreement with the aeroelastic code HAWC2 [4]. Later, Gaunaa et al. [5] also employed CFD methods to correct the engineering model for the DTU 10 megawatt (MW) blade. Kuijken [5] applied CFD and HAWC2 to investigate the critical parameters affecting blade response and provided hoisting recommendations. Zhao et al. [6] developed an analysis tool for blade installation purposes and identified characteristics of a blade installation system. However, their work focused on the blade responses and did not consider the mating process.

For single blade installations, the mating process is a critical phase when a blade is gradually docked into the hub, and the blade responses are controlled by tugger lines. Fig. 1 illustrates two examples of such mating processes. According to industrial experiences, significant motion of the hub at the monopile top is another important source of wait times, in addition to the blade motion. A possible explanation is that the first bending mode of the monopile structure is usually close to the wave spectral peak period in operational sea states, and the aerodynamic damping of the structure is small. The efficiency of the mating process is closely correlated with the installation cost. For offshore wind farms, there is a tendency to place the support structures in water depths exceeding 40 m. Monopile foundations, if used, can experience significant wave-induced responses.

For this type of marine operation and based on the recommendations given by DNV [9], offshore blade installations can be limited by both the sea state and the wind speed. It is preferable to perform the operations in good weather with low sea states ($H_s \leq 2$ m) and little winds. However, the weather window is often restricted to a few months in the summer. As the wind industry seeks to undertake the blade installations throughout the year, stronger winds and waves are expected. This study selects a representative installation model and performs time-domain simulations under wind-wave conditions with a 1-year return period in addition to reference conditions with a higher probability of occurrence. We attempt to answer the following questions: how can rough environmental conditions affect the alignment and mating process, and is blade motion or hub motion is more critical for an offshore installation?

2. Description of the single blade installation

2.1. Installation procedure

Single blade installations are often carried out by use of a jack-up installation vessel. Once the jack-up vessel is in position, individual blades are lifted up and attached to the hub one by one. A simplified flowchart of the

procedure used by installation contractors is illustrated in Fig. 2. Special tools are often developed by turbine manufacturers to rotate the turbine hub to a horizontal position in step 2. Then, a yoke is used to grab the blade and lift it to the hub level (steps 3 and 4). The blade-root motion is to be monitored at the alignment phase (step 5). If the motion is too large, the blade will be kept hanging close to the hub until the weather condition improves. If, after a certain period, the condition is still too harsh, the blade-yoke system will be lowered to the deck (step 10). The maximum waiting time is assumed to be 30 minutes here. When the relative motion satisfies the requirement, the blade root and hub can be well aligned with manual work. The mating phase then initiates, and the guide pin attached to the blade root will enter the flange hole at the hub (step 6). If this process is successful, the blade will be bolted onto the hub, and the lifting gear will be retracted (step 8).

2.2. Alignment phase

As illustrated by Fig. 3(a), a jack-up vessel with cranes is used for blade installation. The alignment phase does not initiate until the blade is lifted to the hub height. By slewing the crane and adjusting the tugger lines, the blade root is brought closer to the hub location. Fig. 3(b) shows two possible scenarios during the alignment. In the figure, R_b and R_h represent the radius of the blade root and of the hub, respectively. D is the distance between the centers. At this stage, the blade root and the hub may experience relative motions, and the distance is a function of time. If $D > R_b + R_h$, the excursions are too large, and the alignment cannot be done. However, if at another time instant, $D < R_b + R_h$, it is possible to align the blade center with the hub center under visual and manual assistance. Based on this assumption, we can follow the relative motion between the two centers in the yz-plane, and calculate the motion outcrossing numbers of the circular boundary with radius R_{sb1}. For a given period of time, if the outcrossing rate is low enough, the alignment is likely to be successful.

2.3. Mating phase

After aligning the blade root and hub, the mating phase initiates. Fig. 4(a) illustrates the main components of the blade root and hub. The bolts can be of the type "T-bolts", which are inexpensive and commonly used for blade root connections [10]. The guide pin is longer than the bolts and will go through a flange hole first. The bolts can then be smoothly mated with flange holes. The criteria for successful mating should be more stringent than that for the alignment phase. As shown in Fig. 4(b), there can be two scenarios of interest. Here, D still represents the distance between the two centers, and R_{fh} and R_p represent the motion radius of the flange hole and of the guide pin, respectively. If D exceeds $R_{fh} - R_p$, mating is not possible. In contrast, if $D < R_{fh} - R_p$, mating can take place. Based on this assumption and to evaluate the success rate in a probabilistic manner, we also follow the relative motions between the centers of the guide pin and flange hole in the yz-plane, and calculate the motion outcrossing numbers of the circular boundary with radius R_{sb2}. In practice the low-frequency part of the relative motions can be controlled, and the effect should depend on the characteristics of the winches that run tugger lines. In this work, only the frequency components higher than 0.5 Hz are assumed to be relevant for the mating phase. For a given period of time, if the outcrossing rate of the high-frequency relative motion is below a certain threshold, the mating process is deemed successful. This requirement is analogous to the one during offshore installation of transition pieces [11].

3. Approach

3.1. Structural modeling

The structural formulation of HAWC2 is based on a multibody system [4]. The structure is divided into a number of independent coupled objects. Although large translations and rotations are allowed at the coupling joint, small deflections are assumed within each object. In this work, the first structural model consists of a monopile foundation, a tower structure, a nacelle, and three hubs. Each body is modeled as a sequence of Timoshenko beam elements and fixed to each other.

Fig. 5 illustrates the second structural model, which consists of a blade, a lift wire, two sling wires, and two tugger lines. The blade is treated as one single body. One end of the lift wire and the tugger lines is connected to the crane. The crane boom and the jack-up vessel are considered as one rigid body fixed to the seabed. In fact, the crane flexibility could be considered, and the connection to the seabed of the jack-up might not be rigid. Each tugger line is 10 m long and comprises cable bodies 1 m in length that are connected by spherical joints. The spherical joints allow relative rotations between connecting bodies. By doing so, one is able to model the noncompressive tugger lines. The yoke weight is modeled as a concentrated mass acting at the center of mass of the blade.

3.2. Soil-pile interaction

Fig. 6 illustrates the monopile foundation with the soil profile. A layered soil profile is considered with soil density increasing with depth [12]. The distributed springs model is used for the pile foundation. This model idealizes the monopile with flexible foundation as a free-free beam with lateral (Winkler-type) springs distributed along the subsoil portion of the monopile [13].

3.3. Wind and aerodynamic model

Deterministic and stochastic wind conditions are available in HAWC2. The deterministic part of the wind includes features such as mean wind velocity, a linear trend, and special shears. The stochastic wind usually refers to the turbulence model. In this work, Mann's turbulence model was applied. Mann's model is based on isotropic turbulence in neutral atmospheric conditions but accounts for non-isotropic turbulence by using the rapid distortion theory [14]. A length scale factor L, an eddy lifetime constant Γ, and a spectral multiplier ($\alpha\epsilon^{2/3}$) are used to generate the turbulence box.

For the case of a nonrotating blade, the steady aerodynamic lift and drag coefficients are used to determine the wind loads on each blade section. The cross-flow principle [15] is applied in HAWC2, which considers the flow to be 2-dimensional (2-D) and ignores wind components in the spanwise direction. This approach is generally applicable to situations without yaw but may require CFD corrections for yawed flow [5]. The dynamic stall model does not strongly affect the blade behavior [16] and is not used in this work.

3.4. Hydrodynamic loads

The hydrodynamic loads in HAWC2 are calculated by Morison's formula, which is composed of inertial and drag terms. For a moving cylinder, the hydrodynamic force per unit length normal to each strip can be expressed as

$$f_s = \rho C_M \frac{\pi D^2}{4} \ddot{x_w} - \rho (C_M - 1) \frac{\pi D^2}{4} \ddot{\eta}_1 + \frac{1}{2} \rho C_D D (\dot{x}_w - \dot{\eta}_1) |\dot{x}_w - \dot{\eta}_1| \tag{1}$$

where C_M and C_D are the mass and drag coefficients, respectively. $\dot{x}_w$ and $\ddot{x}_w$ are the velocity and acceleration of a water particle at the strip center. $\dot{\eta}_1$ and $\ddot{\eta}_1$ are the velocity and acceleration, which are small for monopile foundations. In Eq. (1), the first term includes the Froude-Kriloff (FK) and diffraction force, the second term is the inertial force, and the last term is the quadratic drag force [17]. For support structures of offshore wind turbines with characteristic diameters of 3 to 5 m, the inertial force is dominant [18]. The drag coefficients are dependent on the KC number, Reynolds number, and surface roughness [9] and cannot be determined accurately. In this work, C_M and C_D are selected as 2.0 and 1.0, respectively.

3.5. Metocean conditions

The "North Sea Center" site is selected as a potential site for an offshore wind farm. This site is located in the North Sea, with an average water depth of 29 m and an average wind power density of 871 W/m^2 [19]. Based on 10 years of hindcast data, the long-term joint distribution of the mean wind speed U_w, significant wave height H_s, and wave peak period T_p can be written as

$$f_{Uw,Hs,Tp}(u,h,t) = f_{Uw}(u) \cdot f_{Hs|Uw}(h|u) \cdot f_{Tp|Uw,Hs}(t|u,h) \tag{2}$$

where the marginal distribution of U_w can be fitted by a two-parameter Weibull distribution as

$$f_{Uw}(u) = \frac{\alpha_U}{\beta_U}(\frac{u}{\beta_U})^{\alpha_U - 1} \cdot exp[-(\frac{u}{\beta_U})^{\alpha_U}] \tag{3}$$

where α_U and β_U are the shape and scale parameters, respectively. Given U_w, the conditional probability density function of H_s also can be fitted by a two-parameter Weibull distribution:

$$f_{Hs|Uw}(h|u) = \frac{\alpha_{HC}}{\beta_{HC}}(\frac{h}{\beta_{HC}})^{\alpha_{HC} - 1} \cdot exp[-(\frac{h}{\beta_{HC}})^{\alpha_{HC}}] \tag{4}$$

where α_{HC} and β_{HC} denote the shape and scale parameters, respectively. The conditional distribution of T_p given U_w and H_s can be fitted by a lognormal distribution:

$$f_{Tp|Uw,Hs}(t|u,h) = \frac{1}{\sqrt{2\pi}\sigma_{ln(T_p)}t} \cdot exp\Big[-\frac{1}{2}(\frac{ln(t) - \mu_{ln(T_p)}}{\sigma_{ln(T_p)}})^2\Big] \tag{5}$$

where $\mu_{ln(T_p)}$ and $\sigma_{ln(T_p)}$ are the parameters in the conditional lognormal distribution.

Based on Eq. (2), the 1-year combinations of the variables are located on a sphere of radius r given by

$$\Phi(r) = 1 - \frac{1}{N_1} \tag{6}$$

where $\Phi()$ is the probability density function of the standard normal distribution, and N_1 is the total number of 30-minute sea states in one year. The 1-year contour surface of U_w, H_s, and T_p can be obtained by transforming this sphere back to the physical parameter space.

4. Case study

4.1. System description

The present installation system consists of two structural models. The first model includes the pre-assembled monopile, tower, nacelle, and hubs. This model adapts the phase II model of the Offshore Code Comparison

Collaboration (OC3) Project [13], which includes realistic soil properties. In the original OC3 model, the damping ratio of the first fore-aft and side-side modes is approximately 0.2%. To make the value more realistic, we calibrated the soil damping factor and increased the damping ratio to 1%, based on [20, 21].

The second model includes the NREL 5 MW blade [22] with realistic yoke and tugger line properties. The tugger lines have constant lengths and varying tensions. Table 1 lists key parameters of the system. The natural periods of the system are obtained by an eigenvalue analysis. For the blade structure, the leading edge is facing downward. The choice of this orientation is primarily due to concerns for transport and lifting tools. Although this blade pitch of -90 deg does not have the minimum mean loading compared to other blade pitches, e.g. 0 deg, the loading is more predictable when the wind direction changes [16]. Tugger lines 1 and 2 are equidistant from the blade mass center; see Fig. 5. During the simulations, the blade and hub have no contacts with each other, regardless of their overlaps in the yz-plane. In reality, the mating phase can be affected by the forces from the manual operation using a guide wire. This aspect is not considered in the simulations.

Table 1: Main properties of the components

Parameter	*Symbol*	*Value*
Monopile-tower-nacelle assembly		
Monopile diameter (m)	D_m	6
Monopile penetration (m)	P_m	36
Natural period of the 1st fore-aft mode (s)	T_{FA}	3.85
Damping ratio of the 1st fore-aft mode	ζ_{FA}	1%
Blade-yoke-tugger line system		
Blade mass (tons)	M_{bd}	17.3
Blade length (m)	L_{bd}	61.5
Blade root diameter (m)	D_{bd}	3.54
Yoke weight (ton)	W_{yk}	20
Position of the blade mass center (m)	Xb_{COG}	20.57
Tugger line length (m) [23]	L_{tl}	10
Tugger line stiffness (kN/m)	K_{tl}	$2.0 \cdot 10^5$
Tugger line unit weight (kg/m)	W_{tl}	306
1st rotational mode about the y-axis (Hz)	f_{r1}	0.04
1st translational mode in the y-direction (Hz)	f_{t1}	0.11

4.2. Load cases

To investigate the limiting conditions for the installations, we select relatively rough environmental conditions. Table 2 summarizes the load cases, where EC stands for environmental condition, U_w denotes the mean wind speed at 10-m height, TI denotes turbulence intensity, β_{wave} represents wave heading, and De represents water depth. The mean wind speed of 14 m/s is close to the known upper limit. The nature of offshore wind is turbulent, and wind turbine design standards suggest correlations between turbulence intensity and mean wind speed [24]. For the

sake of simplicity, two turbulence intensities are considered, which are indicative of low and high turbulence. For each U_w, three points of H_s and T_p are of 1-year return period, and 1 point has the expected values of H_s and T_p from their conditional distributions. Fig. 7(a) shows an example for U_w=14 m/s. Among the four points, point A has the largest H_s, points B and C have T_p close to the first fore-aft natural period of the tower (T_{FA}), and point D has a higher probability of occurrence. The hindcast data indicate that most of the wave-wind misalignments are less than 60 deg (Fig. 7(b)). Therefore, the wave misalignment is limited to 60 deg in this study.

Table 2: Environmental conditions with wind-wave misalignment

EC	Point	U_w [m/s]	*TI*	H_s [m]	T_p [s]	β_{wave} [deg]	*De* [m]
1	A	6	0.06, 0.12	2.87	6.03	0, 30, 60	25, 40
2	B	6	0.06, 0.12	2.24	3.86	0, 30, 60	25, 40
3	C	6	0.06, 0.12	0.05	3.89	0, 30, 60	25, 40
4	D	6	0.06, 0.12	1.29	7.33	0, 30, 60	25, 40
5	A	8	0.06, 0.12	3.28	5.61	0, 30, 60	25, 40
6	B	8	0.06, 0.12	2.59	3.85	0, 30, 60	25, 40
7	C	8	0.06, 0.12	0.10	3.87	0, 30, 60	25, 40
8	D	8	0.06, 0.12	1.72	7.25	0, 30, 60	25, 40
9	A	10	0.06, 0.12	3.56	5.23	0, 30, 60	25, 40
10	B	10	0.06, 0.12	2.87	3.85	0, 30, 60	25, 40
11	C	10	0.06, 0.12	0.21	3.84	0, 30, 60	25, 40
12	D	10	0.06, 0.12	2.20	7.29	0, 30, 60	25, 40
13	A	12	0.06, 0.12	3.77	4.99	0, 30, 60	25, 40
14	B	12	0.06, 0.12	3.09	3.84	0, 30, 60	25, 40
15	C	12	0.06, 0.12	0.40	3.88	0, 30, 60	25, 40
16	D	12	0.06, 0.12	2.73	7.41	0, 30, 60	25, 40
17	A	14	0.06, 0.12	3.89	4.78	0, 30, 60	25, 40
18	B	14	0.06, 0.12	3.26	3.86	0, 30, 60	25, 40
19	C	14	0.06, 0.12	0.67	3.82	0, 30, 60	25, 40
20	D	14	0.06, 0.12	3.30	7.60	0, 30, 60	25, 40

4.3. Time-domain simulations

Simulations were performed with a time step of 0.01 seconds (s). For each case in Table 2, six 30-minute simulations with random wave and wind seeds were performed to reduce statistical uncertainties. Each simulation lasted 2400 s, and the start-up transients (600 s) were discarded in the postprocessing.

5. Results and discussions

The response statistics are based on an average of six simulations for each case. The y- and z-directions below refer to the earth-fixed global coordinate system.

5.1. Alignment phase

A few metrics are defined to quantify the outcrossing rate of the blade, hub, and relative motions. The safe boundary, R_{sb1}, is equivalent to the blade-root diameter. The critical outcrossing rate, ν_{cr1}, is the allowable

outcrossing rate for a successful alignment; its calculated value is $5.5 \cdot 10^{-3}$ Hz, which is equivalent to one outcrossing per three minutes. η_{cr1} is the critical motion radius derived from ν_{cr1}. The alignment attempt is deemed successful, if Eq. (7) is satisfied.

$$\eta_{cr1} \leq R_{sb1} \tag{7}$$

5.1.1. Blade-root motion

The blade motion is affected by wind excitations and the tugger line properties. As indicated by Fig. 8, when subjected to wind excitations (regardless of wind speed or turbulence intensity), the blade root moves into the wind. Because of greater loads on the outboard part, the blade has a mean yaw about the z-direction. The aerodynamic angle of attack nears 90 deg. Because of the drag-type wind loads, the displacements in the y- and z-directions of the blade root are Gaussian. The root displacement in the x-direction is small and is considered less important for the alignment process. Fig. 9(a) shows the positions of the blade-root center in the yz-plane during a 30-minute simulation. The root displacement in the wind direction is dominant, and the y- and z-displacements are correlated. The dominant resonant modes of the blade-yoke system can be identified in Fig. 9(b). The first rotational mode, or the pendulum mode (f_{r1} in the figure), makes an important contribution to the blade-root motion in the y-direction. This observation is also reported by Zhao et al. [6]. For U_w=10 m/s and TI=0.12, five outcrossings out of the safe boundary are observed during 30 minutes time (Fig. 9(c)). Fig. 9(d) plots the relation between the ν and η_b by using the time series of the blade-root motion radius. The level of ν_{cr} is not too low, and η_{bcr} is obtained by interpolating existing data. As Eq. (7) is satisfied in this case, the alignment process would be successful if the blade motion alone were of concern.

The blade-root motion radius is the instantaneous distance between the root center and the mean position. Table 3 gives statistics for the cases with TI=0.06. As indicated by the skewness and kurtosis, the root motion radius is nonGaussian, and the mean, maximum, and standard deviation scale quadratically with U_w. This observation is expected because the integrated aerodynamic force F_y is proportional to U_w^2; see Eq. (8). Here, dF_y is the cross flow drag force for a length dx. ρ is air density, U is the inflow wind speed, c is the cord length of the airfoil section, and C_d is the 2-D aerodynamic drag coefficient.

$$dF_y = \frac{1}{2}\rho U^2 c C_d dx \tag{8}$$

As shown in Fig. 10, the blade-root critical motion radius also scales quadratically with the mean wind speed. This trend applies to the cases with TI=0.12, too. For a given wind speed, η_b is linearly proportional to TI because of correlations with standard deviations of the blade root motion. This trend is also reported by the wind force linearization approach [2]. For the cases with low turbulence (TI=0.06), η_b will not exceed $R_{sb} = 3.54$ m until U_w reaches 18.5 m/s, whereas for the cases with high turbulence (TI=0.12), η_b exceeds R_{sb} when U_w is above 12 m/s.

5.1.2. Hub motion

Unlike the blade-root responses, the hub motion is governed by wave loads and is sensitive to sea state, wave misalignment, and water depth. Fig. 11(a) shows a typical time history of the hub center movements, when the monopile foundation is subjected to collinear wind and waves at 40-m water depth. Even for T_p=5.61 s, the y-displacement of the hub is dominated by the first fore-aft mode of the tower (Fig. 11(b)). It is approximately

Table 3: Statistics of the blade-root motion radius, average of six 30-minute simulations, TI=0.06

EC	U_w [m/s]	Mean [m]	Max [m]	Std [m]	Skewness	Kurtosis
1, 2, 3, 4	6	0.21	0.82	0.15	0.94	3.51
5, 6, 7, 8	8	0.33	1.26	0.23	1.01	3.83
9, 10, 11, 12	10	0.48	1.88	0.35	1.03	3.87
13, 14, 15, 16	12	0.66	2.65	0.47	1.03	3.96
17, 18, 19, 20	14	0.87	3.35	0.60	0.97	3.83

Gaussian distributed. The hub motion radius measures the excursion of the hub center from its mean position, and does not outcross the red dashed line in Fig. 11(c) over this simulation. Similar to the blade critical motion radius, the hub critical motion radius, η_{hcr}, can be obtained by interpolating η_h and ν. As shown in Fig. 11(d), the derived η_{hcr} is less than R_{sb}. Under the assumption that R_{sb} is acceptable, the alignment would be successful if the hub motion alone is accounted for. The conclusion is likely to be different if T_p moves closer to T_{FA} or if the blade-root motion is considered in the analysis.

Table 4 summarizes the response statistics of the hub motion radii for the collinear cases. As indicated by the kurtosis values, hub motion radius is nonGaussian and different from the hub y-displacement. Among the four sea states for a given wind speed, points B (EC 2, 6, ...,18) always have the largest mean, maximum, and standard deviation, and the maximum values can be more than twice those of points A, which have higher H_s and T_p. For ECs with T_p close to T_{FA}, the mean, max, and standard deviation all increase with H_s. These statistics represent the worse-case responses of the hub motion during installations. If De reduces to 25 m, or if β_{wave} increases, the response magnitudes also decrease, but the trend is similar.

We investigate the effects of water depth and wave misalignment by using the critical motion radius metric. As shown in Fig. 12(a), water depth has a significant impact on η_{hcr}. When De=25 m and β_{wave}=0 deg, the hub motion is within the safe boundary for all ECs. When De rises to 40 m, η_{hcr} has doubled for many ECs, but only those of points B exceed the safe boundary. For points D with higher probabilities of occurrence, η_{hcr} reaches 0.5 m and 1.8 m for 25- and 40-m water depths, respectively, under the largest waves (EC 20). Hence, installations of monopile wind farms at greater water depth should raise particular concerns.

For β_{wave} other than 0 deg, the percentage reduction in η_{hcr} can be defined as

$$PR = \frac{\eta_{cr}(0) - \eta_{cr}(\beta)}{\eta_{cr}(0)} \times 100\ \% \tag{9}$$

where $\eta_{cr}(\beta)$ stands for the critical motion radius for wave heading β.

In Fig. 12(b), regardless of the water depth, the reduction is uniform across the ECs: approximately 49% and 13% for β_{wave}=30 deg and β_{wave}=60 deg, respectively. This observation is intuitive, because the long-crested waves lose energy in the y-direction by (1-cos(β_{wave})); the effect propagates to the monopile motions at the top. According to the hindcast data, β_{wave} is less than 30 deg most of the time, so the reduction in η_{hcr} due to wave misalignment would be limited.

Table 4: Statistics of the hub motion radius, average of six 30-minute simulations, TI=0.06, De=40 m, β_{wave}=0 deg

EC	H_s [m]	T_p [m]	Mean [m]	Max [m]	Std [m]	Skewness	Kurtosis
1	2.87	6.03	0.48	2.28	0.37	1.19	4.66
2	2.24	3.86	1.16	5.28	0.97	1.41	5.21
3	0.05	3.89	0.02	0.07	0.01	0.97	3.70
4	1.29	7.33	0.23	0.90	0.17	0.91	3.33
5	3.28	5.61	0.56	2.46	0.43	0.97	3.60
6	2.59	3.85	1.37	5.31	1.09	0.91	3.18
7	0.10	3.87	0.04	0.14	0.02	0.91	3.58
8	1.72	7.25	0.32	1.38	0.23	0.87	3.53
9	3.56	5.23	0.67	2.72	0.48	0.89	3.61
10	2.87	3.85	1.48	5.68	1.18	0.98	3.38
11	0.21	3.84	0.07	0.31	0.05	0.92	3.48
12	2.20	7.29	0.40	1.87	0.29	1.05	4.36
13	3.77	4.99	0.75	2.78	0.55	0.76	2.91
14	3.09	3.84	1.56	6.15	1.23	0.92	3.23
15	0.40	3.88	0.14	0.64	0.11	1.39	5.48
16	2.73	7.41	0.44	1.98	0.32	1.04	4.29
17	3.89	4.78	0.80	3.44	0.61	0.91	3.54
18	3.26	3.86	1.62	6.17	1.25	0.91	3.26
19	0.67	3.82	0.24	1.00	0.19	1.08	3.83
20	3.30	7.60	0.46	2.10	0.34	1.06	4.18

5.1.3. Relative motion between blade root and hub

As shown above, either the blade root or the hub may encounter excessive motions. Relative motion between the two bodies is more relevant in realistic situations and will be analyzed in this section.

The spectra of the motion radii indicate the response standard deviations and hence the relative importance of the blade-root or hub motions. EC18 is the roughest condition among the ECs and is selected as the representative case. The sharp peaks of the hub motion radius in Figs. 13(a)–13(b) are close to 0.54 Hz and come from the first fore-aft mode. The spectral densities of the blade motion radius are concentrated in the low frequency region (<0.2 Hz). When De=25 m, the monopile resonant responses are less significant compared to the wind-induced blade motions, whereas the monopile resonant peak becomes prominent and makes considerable contribution to the hub motion standard deviation for De=40 m.

Fig. 14 compares the blade-root, hub, and relative motion radii for EC18. For the given ν_{cr} level in Fig. 14(a), η_{hcr} is 2.3 m less than η_{bcr}, which amounts to 83% of the relative motion radius η_{rcr}. When De=40 m and T_p is near T_{FA}, η_h becomes greater than η_b. η_{hcr} and η_{bcr} accounts for 57% and 77% of η_{rcr}, respectively. Note that the curve of the hub motion has the steepest slope. For lower outcrossing rate, it is likely that the blade-root motion becomes more important, and extrapolation methods [25] may be involved to obtain the critical motion radius.

Fig. 15 displays the main effects of four variables on the mean value of η_{rcr} across all factor levels. The magnitude of the main effect increases with the slope of the line. The effects of mean wind speed and turbulence intensity on the blade-root motion and the effects of water depth and wave misalignment on the hub motion are reflected in the relative motion. The mean value of η_{rcr} increases linearly with TI and quadratically with U_w and decreases sinusoidally with β_{wave}.

For the specified ν_{cr}, η_{rcr} always exceeds η_{bcr} and η_{hcr}. To measure the relative importance of the blade and hub motions, we compare the critical motion radii across the ECs. Figs. 16(a)–16(b) represent the conditions with TI=0.12 and β_{wave}=0 deg. When De=25 m and for points A, η_{bcr} often exceeds η_{hcr}, accounting for 75%–93% of η_{rcr}. Compared to points A, H_s of points D is less, but T_p is larger. Thus, the weight of η_{bcr} further increases, accounting for 84%–95% of η_{rcr}. For points B, T_p is close to T_{FA}, and both the blade and hub motions are important, with η_{bcr} ranging from 49% to 79% of η_{rcr} at U_w=6 m/s and 14 m/s, respectively, and η_{hcr} reducing from 77% to 38% of η_{rcr}. For points C, because H_s is small, only the blade motion is important, η_{bcr} accounting for more than 95% of η_{rcr}. Compared to De=25 m, the hub motion plays a more important role when De=40 m. As shown in Fig. 16(b), for points A, η_{hcr} reaches 87% and 52% of η_{rcr} at U_w=6 m/s and 14 m/s, respectively. η_{bcr} accounts for a maximum of 72% at U_w=14 m/s. For points B, the hub motion is more important, η_{hcr} ranging from 93% to 77% of η_{rcr} at U_w=6 m/s and 14 m/s, respectively. For points C, the blade motion is still more important across the mean wind speeds. For points D, the blade and hub motions are equally important at U_w=6 m/s. When U_w=14 m/s, the blade motion dominates, and η_{bcr} and η_{hcr} equal 81% and 34% of η_{rcr}, respectively.

Figs. 16(c)–16(d) compare the critical motion radii for the conditions with wave misalignment and reduced wind turbulence. From Sections 5.1.1 and 5.1.2, it is revealed that for TI=0.06 and β_{wave}=30 deg, η_{bcr} is reduced by 50% and η_{hcr} by 13% in comparison with the collinear conditions with TI=0.12. Hence, η_{hcr} is expected to be more important than before. Still, when De=25 m and for points A, η_{hcr} is exceeded by η_{bcr} when U_w is above 8 m/s. For points C and D, η_{bcr} is always larger than η_{hcr}. The observation differs when De=40 m. Because of

the increased wave-induced vibrations, η_{hcr} consistently exceeds η_{bcr} for points A and B. In those cases, using η_{hcr}, instead of η_{rcr}, would cause an underestimate of 20% for $U_w \leq$10 m/s. For points C, the blade motion is dominant. For points D, the blade motion is more important for $U_w \geq$12 m/s.

To assess the successfulness of the blade alignment process by using a single parameter (η_{cr}), the three critical motion radii are compared against the safe boundary in Fig. 16. The results are summarized in Tables 5–6. Whenever an "N" is registered for either η_{bcr} or η_{hcr}, an "N" will appear for η_{rcr} too. Nevertheless, a "Y" for both η_{bcr} and η_{hcr} will not be necessarily associated with a "Y" for η_{rcr}. When De=25 m and TI=0.12, 13 out of 20 ECs are successful with a "Y" for η_{rcr}. Among the successful cases, EC16 belongs to points D with higher probability of occurrence. It has a mean wind speed of 12 m/s. When TI=0.06 and β_{wave}=30 deg, all ECs are successful. Compared to De=25 m, the success rate of De=40 m is appreciably lower: 9 out of 20 when TI=0.12 and β_{wave}=0 deg and 14 out of 20 when TI=0.06 and β_{wave}=30 deg. For the former condition, no cases of points B are successful, and EC12 is successful, corresponding to the roughest condition of points D. For the latter condition, all cases of points D are successful.

It is nonconservative to consider the blade motion (η_{bcr}) alone for decision making, especially when the blade-root motions are less important (De=40 m and TI=0.06). On the other hand, neither will the hub motion (η_{hcr}) alone give predictions accurately, especially for conditions with shallow water depth and high turbulence (De=25 m and TI=0.12).

5.2. Mating phase

The outcrossing rates of the guide pin, flange hole, and their relative motions are of interest to the mating phase. The safe boundary, R_{sb2}, is defined as the difference between the flange-hole radius and the guide-pin radius, i.e., $R_{sb2} = R_{fh} - R_p$. Common flange-hole diameters vary between 16 mm to 48 mm, and R_{sb2} is taken as 4 mm in the following. The critical outcrossing rate, ν_{cr2}, is the allowable outcrossing rate for a successful mating; its calculated value is $1.67 \cdot 10^{-2}$ Hz, which is equivalent to one outcrossing per minute. This outcrossing rate is a representative value based on experience [23]. Because the low-frequency part can be controlled, only the high-frequency components (> 0.5 Hz) of the response signals were used in the postprocessing. The mating process is deemed successful if Eq. (10) is satisfied.

$$\eta_{cr2} \leq R_{sb2} \tag{10}$$

where η_{cr2} is the critical motion radius derived from ν_{cr2}. The actual mating phase lasts a few minutes, and the six 30-minute simulations were still used to obtain the critical motion radius. Thus, statistical uncertainties of the results are expected to be very low.

5.2.1. Motion of guide pin

As the guide pin is assumed to be rigidly connected to the blade root, the motion characteristics of the guide pin in the yz-plane are very similar to those of the blade root. Fig. 17(a) shows a representative time history of the high-frequency response under U_w=10 m/s and De=25 m. As shown, the maximum magnitude is only a few millimeters. The critical motion radius corresponding to the specified outcrossing rate can be interpolated from the

Table 5: Evaluation of the alignment process between blade and hub (Y: successful N: unsuccessful), TI=0.12, β_{wave}=0 deg

EC	U_w [m]	H_s [m]	T_p [s]	De=25 m			De=40 m		
				η_{bcr}	η_{hcr}	η_{rcr}	η_{bcr}	η_{hcr}	η_{rcr}
1	6	2.87	6.03	Y	Y	Y	Y	Y	Y
2	6	2.24	3.86	Y	Y	Y	Y	N	N
3	6	0.05	3.89	Y	Y	Y	Y	Y	Y
4	6	1.29	7.33	Y	Y	Y	Y	Y	Y
5	8	3.28	5.61	Y	Y	Y	Y	Y	Y
6	8	2.59	3.85	Y	Y	Y	Y	N	N
7	8	0.10	3.87	Y	Y	Y	Y	Y	Y
8	8	1.72	7.25	Y	Y	Y	Y	Y	Y
9	10	3.56	5.23	Y	Y	Y	Y	Y	N
10	10	2.87	3.85	Y	Y	N	Y	N	N
11	10	0.21	3.84	Y	Y	Y	Y	Y	Y
12	10	2.20	7.29	Y	Y	Y	Y	Y	Y
13	12	3.77	4.99	Y	Y	N	Y	Y	N
14	12	3.09	3.84	Y	Y	N	Y	N	N
15	12	0.4	3.88	Y	Y	Y	Y	Y	Y
16	12	2.73	7.41	Y	Y	Y	Y	Y	N
17	14	3.89	4.78	N	Y	N	N	Y	N
18	14	3.26	3.86	N	Y	N	N	N	N
19	14	0.67	3.82	N	Y	N	N	Y	N
20	14	3.30	7.60	N	Y	N	N	Y	N

Table 6: Evaluation of the alignment process between blade and hub (Y: successful N: unsuccessful), TI=0.06, β_{wave}=30 deg

EC	U_w [m]	H_s [m]	T_p [s]	De=25 m			De=40 m		
				η_{bcr}	η_{hcr}	η_{rcr}	η_{bcr}	η_{hcr}	η_{rcr}
1	6	2.87	6.03	Y	Y	Y	Y	Y	Y
2	6	2.24	3.86	Y	Y	Y	Y	N	N
3	6	0.05	3.89	Y	Y	Y	Y	Y	Y
4	6	1.29	7.33	Y	Y	Y	Y	Y	Y
5	8	3.28	5.61	Y	Y	Y	Y	Y	Y
6	8	2.59	3.85	Y	Y	Y	Y	N	N
7	8	0.10	3.87	Y	Y	Y	Y	Y	Y
8	8	1.72	7.25	Y	Y	Y	Y	Y	Y
9	10	3.56	5.23	Y	Y	Y	Y	Y	Y
10	10	2.87	3.85	Y	Y	Y	Y	N	N
11	10	0.21	3.84	Y	Y	Y	Y	Y	Y
12	10	2.20	7.29	Y	Y	Y	Y	Y	Y
13	12	3.77	4.99	Y	Y	Y	Y	Y	Y
14	12	3.09	3.84	Y	Y	Y	Y	N	N
15	12	0.40	3.88	Y	Y	Y	Y	Y	Y
16	12	2.73	7.41	Y	Y	Y	Y	Y	Y
17	14	3.89	4.78	Y	Y	Y	Y	Y	N
18	14	3.26	3.86	Y	Y	Y	Y	N	N
19	14	0.67	3.82	Y	Y	Y	Y	Y	Y
20	14	3.30	7.60	Y	Y	Y	Y	Y	Y

relation in Fig. 17(b). In this case, η_{pcr} is well below R_{sb2}, and the mating is successful considering the guide-pin motion alone.

5.2.2. Motion of flange hole

The flange holes are fixed at the hub. Hence, the motion characteristics are same as for the hub and are dominated by the resonant responses. Accordingly, the flange-hole motions are expected to be sensitive to wave loads and insensitive to wind loads. Fig. 18(a) shows the high-frequency responses of a flange-hole under EC5, and Fig. 18(b) presents the relation between the outcrossing rate and the motion radius. Because of the significant wave-induced resonant responses at De=40 m, the critical motion radius η_{fhcr} is excessive compared to the safe boundary. Under such conditions, the mating process is likely to fail.

5.2.3. Relative motion between guide pin and flange hole

The actual success rate of mating is dependent on the relative motion between the guide pin and corresponding flange hole. The high-frequency relative motions of the pair in the yz-plane can be calculated as done similarly for the alignment process. To assess the successfulness of the mating process, the three critical motion radii are compared against the safe boundary R_{sb2} in Fig. 19. For De=25 m and U_w<12 m/s, most critical motion radii of the flange hole and the relative motion are very close; for higher U_w, the guide-pin motions become more important. For De=40 m, the flange-hole motions contribute substantially to the high-frequency responses and govern the mating process. Consequently, most η_{rcr2} are above R_{sb2} and make the high-precision mating process difficult. In Figs. 19(b) and 19(d), some critical motion radii are much higher than 0.01 m and are not shown.

Tables 7–8 summarize the evaluation results of the mating process based on Eq. (10). For De=25 m and β=0 deg, η_{rcr} in 7 out of 20 ECs satisfies the mating criteria. In comparison, for De=40 m and β=0 deg, only two ECs with small wave heights have acceptable η_{rcr}. An increase in the wave misalignment reduces the flange-hole motions in the y-direction, and should influence the mating success rate favorably. For De=25 m, β=30 deg results in two additional ECs with acceptable η_{rcr} compared to β=0 deg. For De=40 m, although a 10% to 20% reduction in η_{rcr} is still observed, the number of successful matings does not increase. By comparing η_{bcr}, η_{hcr}, and η_{rcr}, we see that η_{hcr} can be used for the judgement in most conditions with wind speeds below 12 m/s. To improve the low mating success rate for De=40 m, it may be relevant to redesign the monopile structure with increased stiffness or to implement additional damping devices to the structure.

5.3. Forces in the wires

As shown in Fig. 5, two tugger lines are used to constrain the blade motion. The lift wire, sling wires and tugger lines are all in tension throughout the simulations. Because of the symmetry of the sling wires about the blade mass center, they have tensions in the same range, with mean values of approximately 260 kN and standard deviations less than 8 kN. Tugger line 1 experiences greater loads than line 2 because of the rotational motion of the blade about the z-axis. Nevertheless, the maximum tension in line 1 is less than 110 kN for U_w=14 m/s and TI=0.12. The maximum tugger line tensions are well below the breaking strength and are not discussed further.

Table 7: Evaluation of the mating process between guide pin and flange hole (Y: successful N: unsuccessful), TI=0.12, β_{wave}=0 deg

EC	U_w [m]	H_s [m]	T_p [s]	De=25 m			De=40 m		
				η_{bcr}	η_{hcr}	η_{rcr}	η_{bcr}	η_{hcr}	η_{rcr}
1	6	2.87	6.03	Y	Y	Y	Y	N	N
2	6	2.24	3.86	Y	N	N	Y	N	N
3	6	0.05	3.89	Y	Y	Y	Y	Y	Y
4	6	1.29	7.33	Y	Y	Y	Y	N	N
5	8	3.28	5.61	Y	N	N	Y	N	N
6	8	2.59	3.85	Y	N	N	Y	N	N
7	8	0.10	3.87	Y	Y	Y	Y	Y	Y
8	8	1.72	7.25	Y	Y	Y	Y	N	N
9	10	3.56	5.23	Y	N	N	Y	N	N
10	10	2.87	3.85	Y	N	N	Y	N	N
11	10	0.21	3.84	Y	Y	Y	Y	N	N
12	10	2.20	7.29	Y	Y	Y	Y	N	N
13	12	3.77	4.99	N	N	N	N	N	N
14	12	3.09	3.84	N	N	N	N	N	N
15	12	0.4	3.88	N	Y	N	N	N	N
16	12	2.73	7.41	N	Y	N	N	N	N
17	14	3.89	4.78	N	N	N	N	N	N
18	14	3.26	3.86	N	N	N	N	N	N
19	14	0.67	3.82	N	Y	N	N	N	N
20	14	3.30	7.60	N	Y	N	N	N	N

Table 8: Evaluation of the mating process between guide pin and flange hole (Y: successful N: unsuccessful), TI=0.06, β_{wave}=30 deg

EC	U_w [m]	H_s [m]	T_p [s]	De=25 m			De=40 m		
				η_{bcr}	η_{hcr}	η_{rcr}	η_{bcr}	η_{hcr}	η_{rcr}
1	6	2.87	6.03	Y	Y	Y	Y	N	N
2	6	2.24	3.86	Y	N	N	Y	N	N
3	6	0.05	3.89	Y	Y	Y	Y	Y	Y
4	6	1.29	7.33	Y	Y	Y	Y	N	N
5	8	3.28	5.61	Y	N	N	Y	N	N
6	8	2.59	3.85	Y	N	N	Y	N	N
7	8	0.10	3.87	Y	Y	Y	Y	Y	Y
8	8	1.72	7.25	Y	Y	Y	Y	N	N
9	10	3.56	5.23	Y	N	N	Y	N	N
10	10	2.87	3.85	Y	N	N	Y	N	N
11	10	0.21	3.84	Y	Y	Y	Y	N	N
12	10	2.20	7.29	Y	Y	Y	Y	N	N
13	12	3.77	4.99	Y	N	N	Y	N	N
14	12	3.09	3.84	Y	N	N	Y	N	N
15	12	0.40	3.88	Y	Y	Y	Y	N	N
16	12	2.73	7.41	Y	Y	Y	Y	N	N
17	14	3.89	4.78	N	N	N	N	N	N
18	14	3.26	3.86	N	N	N	N	N	N
19	14	0.67	3.82	N	Y	N	N	N	N
20	14	3.30	7.60	N	Y	N	N	N	N

6. Conclusions

This paper addresses the final installation process of a single blade installation. A monopile model and a 5 MW blade installation model have been developed. The monopile model includes a monopile structure, tower, nacelle, and hubs, and the blade model includes a blade, tugger lines, and a yoke weight. Time-domain simulations were conducted under various wind-wave conditions for a potential wind farm site in the North Sea. By analyzing the motions of the blade root and hub for the alignment process and motions of the guide pin and flange hole for the mating process, the following conclusions are reached:

- The water depth, mean wind speed, turbulence intensity, and wind-wave misalignment are all important to the blade alignment process. For a given outcrossing rate, the derived blade-root motion radius scales quadratically with the mean wind speed and linearly with the turbulence intensity, whereas the derived hub motion radius scales sinusoidally with the wave misalignment. The relations can also be reflected in the relative motion radius between the blade root and the hub.

- For the outcrossing rate of $5.5{\cdot}10^{-3}$ Hz considered in the alignment process, the corresponding blade-root motion radius exceeds the safe boundary of 3.54 m when the mean wind speed is above 12 m/s and the turbulence intensity equals 0.12. The hub motion radius is sensitive to water depth and wave spectral peak period. For the 25-m water depth, the critical hub motion radius is within the safe boundary. For the 40-m water depth, an excessive hub motion radius can occur when the wave peak period is close to the first fore-aft mode of the monopile, which is influenced by soil properties and structural stiffness. Hence, those wave peak periods should always be avoided during blade installation, and additional damping devices may be needed if such operations should occur throughout the year.

- For the alignment process, the relative motion radius is greater than the blade-root motion radius or the hub motion radius. Using the blade-root motion or the hub motion alone, instead of the relative motion, leads to nonconservative predictions for the alignment process. It would be less nonconservative if the blade motion radius alone is used for small waves or if the hub motion radius alone is used for 40-m water depth and under rough sea states.

- The mating process of the guide pin and flange hole requires high precision. An outcrossing rate of $1.67{\cdot}10^{-2}$ Hz and a safe boundary of $4{\cdot}10^{-3}$ m were considered for the high-frequency responses. For the 25-m water depth, the critical motion radius of the flange hole outweighs that of the guide pin for wind speeds below 12 m/s. For the 40-m water depth, the critical motion radius of the flange hole is dominant. For the 25-m water depth and collinear wind and waves, successful mating is possible for 7 out of the 20 environmental conditions investigated, and an increase in the wave misalignment improves mating. For the 40-m water depth, mating can be unsuccessful in realistic sea states.

7. Limitations and future work

The studied installation scenario is a simplification. In reality, the wind direction may change over time, and the scenarios can be more complex. As water depth increases, the monopile penetration depth, diameter and wall

thickness will probably increase together. Strictly speaking, the boundary condition of the crane boom is not entirely fixed. To capture more details of the installation scenario during numerical modelling, it is necessary to collaborate with wind turbine operators. However, the approach presented in this paper can serve as a tool for planning marine operations.

Solutions exist to improve the alignment or mating processes. On the blade side, it is possible to reduce the blade-root motion by controlling the tugger line tensions automatically. An intelligent guidance system may also be used [26]. On the monopile side, wall thickness, diameter, or penetration depth may be adjusted to change the stiffness and natural periods, and passive damping devices [27, 28] can be applied to the structure. The mating success rate can be higher if the annular gap between the guide pin and flange hole increases.

8. Acknowledgements

This work has been financially supported by the Research Council of Norway granted through the Department of Marine Technology and the Centre for Researched-based innovation of Marine Operations, NTNU (RCN project 237929). The authors gratefully acknowledge the support of Thousand Talents Program, NSFC-RCUK_EPSRC Grant, National Natural Science Foundation of China (51479114), The platform construction of ocean energy comprehensive supporting service (2014) (GHME2014ZC01), High-tech Ship Research Projects Sponsored by MIITC Floating Support platform project (201622) and State Key Laboratory of Ocean Engineering at Shanghai Jiao Tong University. The authors thank Oliver Stettner of Global Maritime, Dr. Wilson Guachamin-Acero of Escuela Politecnica Nacional, and the anonymous reviewer for their valuable suggestions. Thanks are extended to Anders Melchior Hansen of DTU Wind Energy and Lukas Kuijken for assistance with HAWC2.

References

[1] Haymarket Media Group Ltd. Ten of the biggest turbines, `http://www.windpowermonthly.com/10-biggest-turbines`, Accessed: Mar 05, 2017.

[2] M. Gaunaa, L. Bergami, S. Guntur, F. Zahle. First-order aerodynamic and aeroelastic behavior of a single-blade installation setup, Journal of Physics: Conference Series 524 (2014) 012073.

[3] Y. Wang, D. Tian, W. He. Computation of hoisting forces on wind turbine blades using computation fluid dynamics, Applied Mechanics and Materials 446 (2014) 452–457.

[4] T. J. Larsen, A. M. Hansen. How 2 HAWC2, the user's manual, Technical Report, Risø National Laboratory, Danmark, 2007.

[5] M. Gaunaa, J. Heinz, W. Skrzypiński. Toward an engineering model for the aerodynamic forces acting on wind turbine blades in quasisteady standstill and blade installation situations, Journal of Physics: Conference Series 753 (2016) 022007.

[6] Y. Zhao, Z. Cheng, P. C. Sandvik, Z. Gao, T. Moan. An integrated dynamic analysis method for simulating installation of a single blade for offshore wind turbines, Ocean Engineering 152 (2017) 72–88.

[7] Siemens AG. Siemens wind turbine blade being positioned, https://www.siemens.co.uk/en/news_press/index/news_archive/2014/siemens-announces-green-port-hull-wind-manufacturing-site-improvements.htm, Accessed: Feb 21, 2017.

[8] RWE AG. Halfway through the turbine installation for the nordsee ost offshore wind farm, HalfwaythroughtheturbineinstallationfortheNordseeOstoffshorewindfarm, Accessed: Feb 21, 2017.

[9] Det Norske Veritas. Recommended practice DNV-RP-H103, modelling and analysis of marine operations, Høvik, Norway, 2014.

[10] M. Peeters, G. Santo, J. Degroote, W. V. Paepegem. The concept of segmented wind turbine blades: A review, Energies 10 (2017) 1112.

[11] W. Guachamin-Acero, T. Moan, Z. Gao. Steady state motion analysis of an offshore wind turbine transition piece during installation based on outcrossing of the motion limit state, in: ASME 2015 34th International Conference on Ocean, Offshore and Arctic Engineering, American Society of Mechanical Engineers, 2015, pp. V003T02A064–V003T02A064.

[12] P. Passon. Memorandum: derivation and description of the soil-pile-interaction models, IEA-Annex XXIIII Subtask 2 (2006).

[13] J. Jonkman, W. Musial. IEA wind task 23 subtask 2 final technical report, Golden, Colorado, USA: National Renewable Energy Laboratory. (2010).

[14] J. Mann. The spatial structure of neutral atmospheric surface-layer turbulence, Journal of Fluid Mechanics 273 (1994) 141–168.

[15] S. F. Hoerner. Fluid-dynamic drag: practical information on aerodynamic drag and hydrodynamic resistance, Hoerner Fluid Dynamics Midland Park, NJ, USA, 1965.

[16] L. Kuijken. Single blade installation for large wind turbines in extreme wind conditions, Master of Science Thesis, Technical University of Denmark & TU Delft (2015).

[17] O. M. Faltinsen. Sea loads on ships and offshore structures, volume 1, Cambridge university press, 1993.

[18] H. Veldkamp. J. Van Der Tempel, Influence of wave modelling on the prediction of fatigue for offshore wind turbines, Wind Energy 8 (2005) 49–65.

[19] L. Li, Z. Gao, T. Moan, Joint distribution of environmental condition at five European offshore sites for design of combined wind and wave energy devices, Journal of Offshore Mechanics and Arctic Engineering 137 (2015) 031901.

[20] M. Damgaard, L. B. Ibsen, L. V. Andersen, J. K. Andersen, Cross-wind modal properties of offshore wind turbines identified by full scale testing, Journal of Wind Engineering and Industrial Aerodynamics 116 (2013) 94–108.

[21] R. Shirzadeh, C. Devriendt, M. A. Bidakhvidi, P. Guillaume, Experimental and computational damping estimation of an offshore wind turbine on a monopile foundation, Journal of Wind Engineering and Industrial Aerodynamics 120 (2013) 96–106.

[22] J. Jonkman, S. Butterfield, W. Musial, Definition of a 5-MW reference wind turbine for offshore system development, Technical Report NREL/TP-500-38060, National Renewable Energy Laboratory, Golden, Colorado, USA (2009).

[23] O. Stettner, Personal communication, Global Maritime, Accessed: January 25, 2017.

[24] International Electrotechnical Commission, IEC 61400-3: Wind turbines–part 3: design requirements for offshore wind turbines (3rd edn.), IEC, Geneva, Switzerland (2009).

[25] A. Næss, O. Gaidai, Estimation of extreme values from sampled time series, Structural Safety 31 (2009) 325–334.

[26] High Wind NV, The boom lock, `http://www.high-wind.eu/boomlock/`, Accessed: Feb 21, 2017.

[27] G. M. Stewart, M. A. Lackner, The impact of passive tuned mass dampers and wind–wave misalignment on offshore wind turbine loads, Engineering Structures 73 (2014) 54–61.

[28] Z. Jiang, The impact of a passive tuned mass damper on offshore single-blade installation, Journal of Wind Engineering and Industrial Aerodynamics 176 (2018) 65–77.

(a)

(b)

Figure 1: (a) Side view of the horizontal single blade mounting on a wind turbine, source: Siemens Wind Power GmbH [7] (b) Bottom view of the horizontal single blade mounting on a wind turbine, source: RWE AG [8]

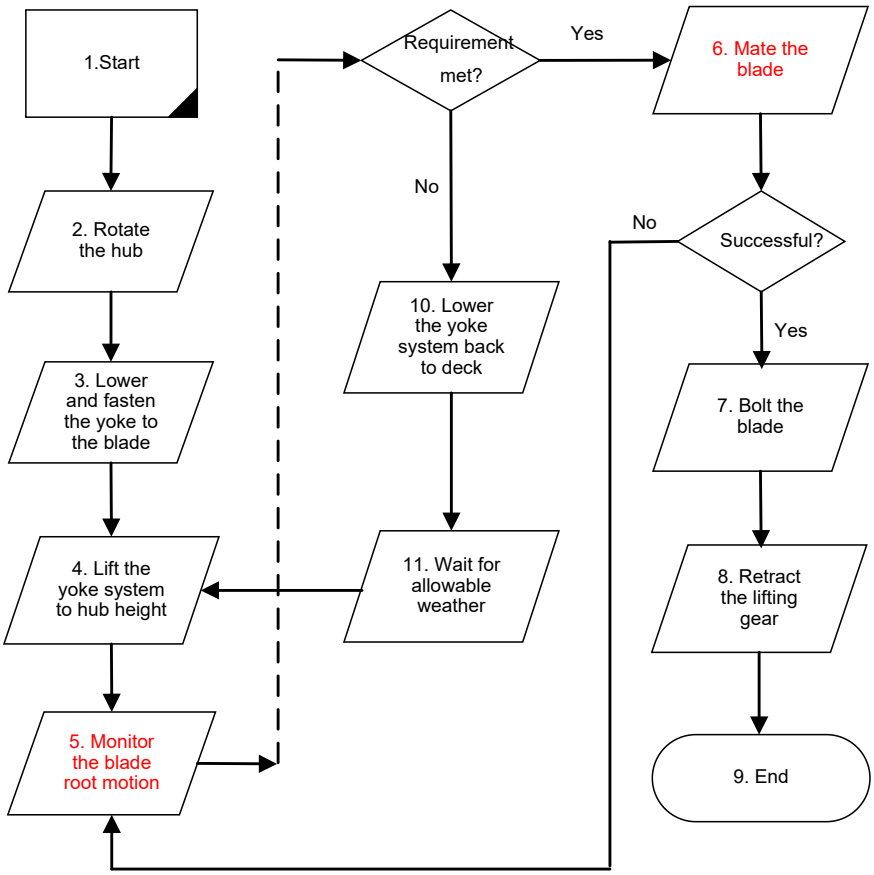

Figure 2: Flowchart of a typical single blade installation

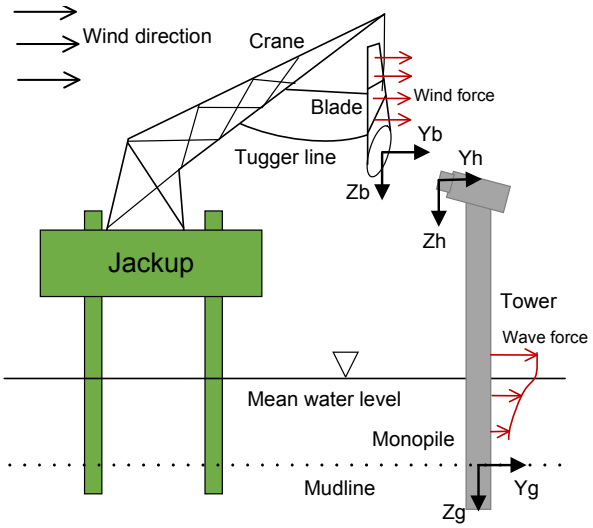

(a)

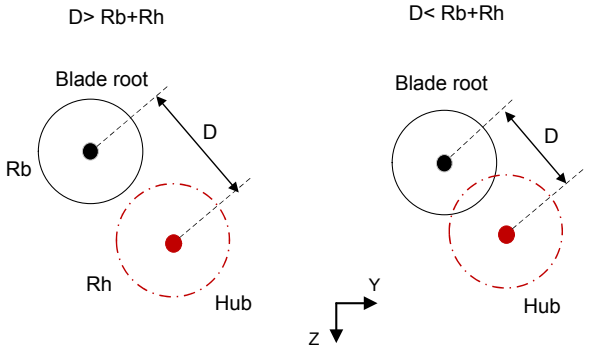

(b)

Figure 3: (a) Schematic of the blade alignment plan for a monopile wind turbine (b) Positions of the blade root and hub in the yz-plane

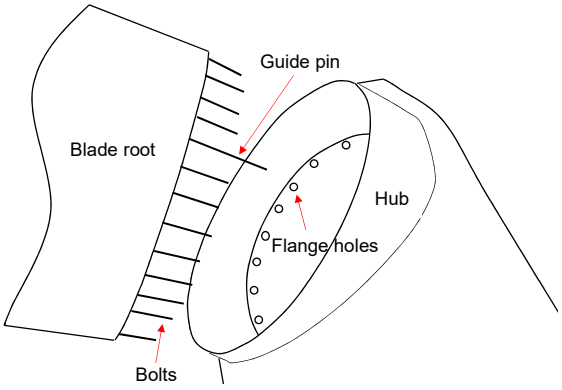

(a)

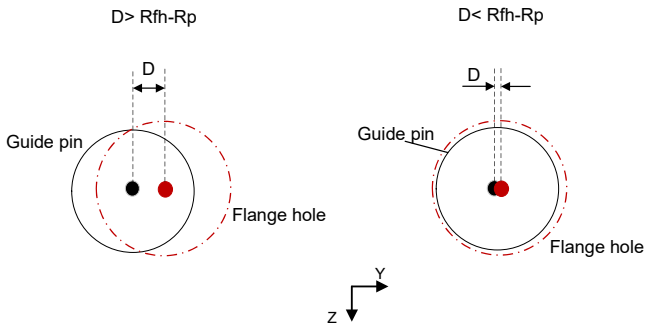

(b)

Figure 4: (a) Schematic of the main components involved in the mating process (b) Positions of the guide pin and flange hole in the yz-plane

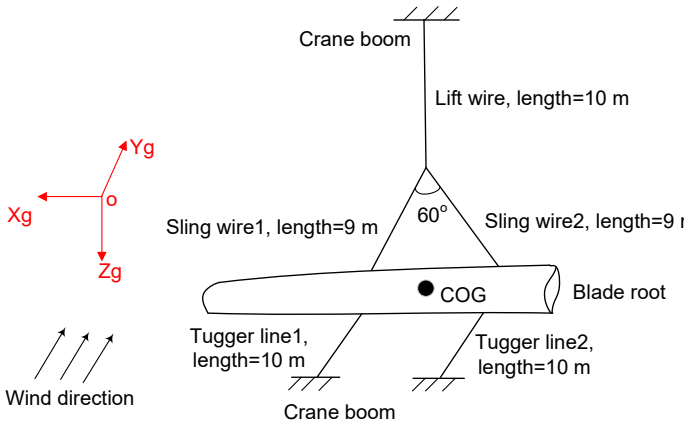

Figure 5: A simplified blade installation model in HAWC2, comprising the blade, tugger lines and yoke weight

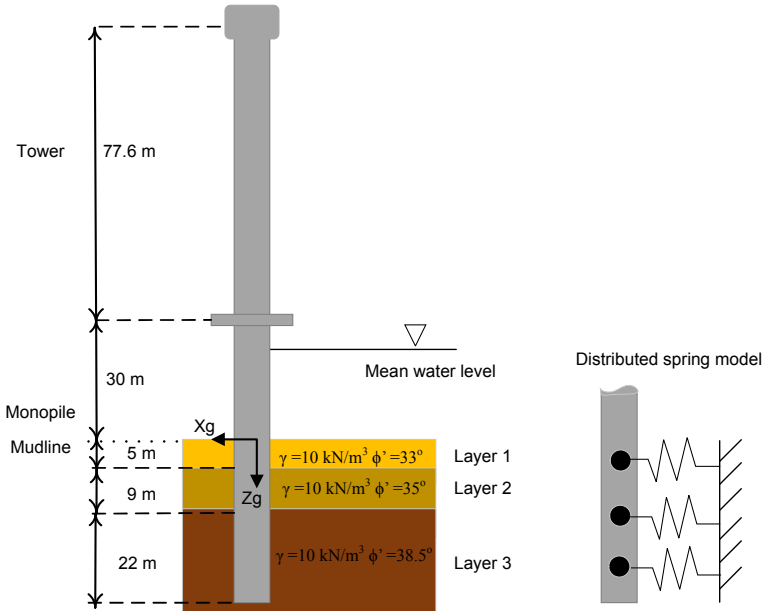

Figure 6: Schematic of the studied monopile model with soil profile

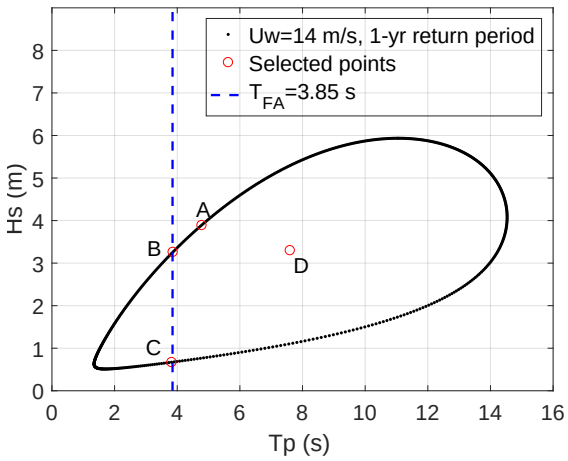

(a)

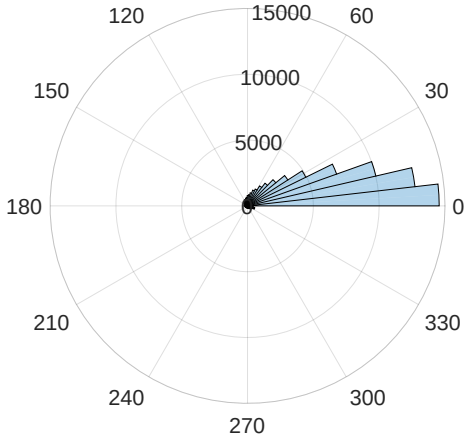

(b)

Figure 7: (a) H_s-T_p contour for U_w=14 m/s, site 15 (b) Polar histogram of the wind-wave misalignment for site 15 during 10 years (2001–2010)

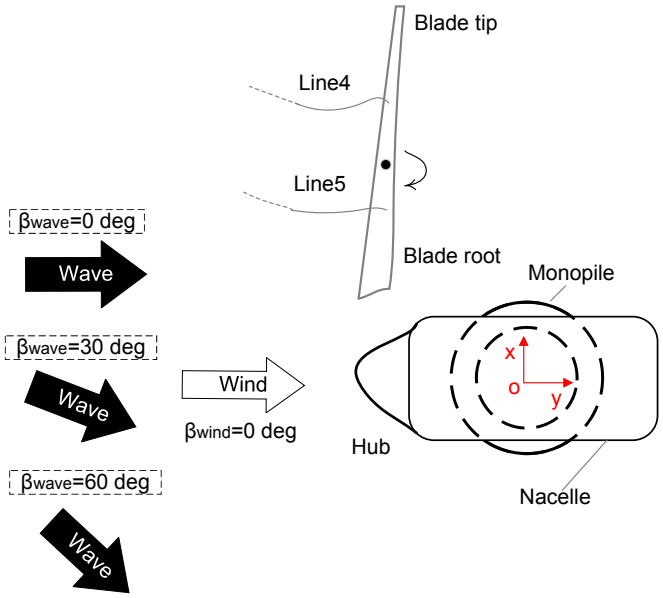

Figure 8: Top view of the blade and the monopile assembly under wind-wave misalignment conditions

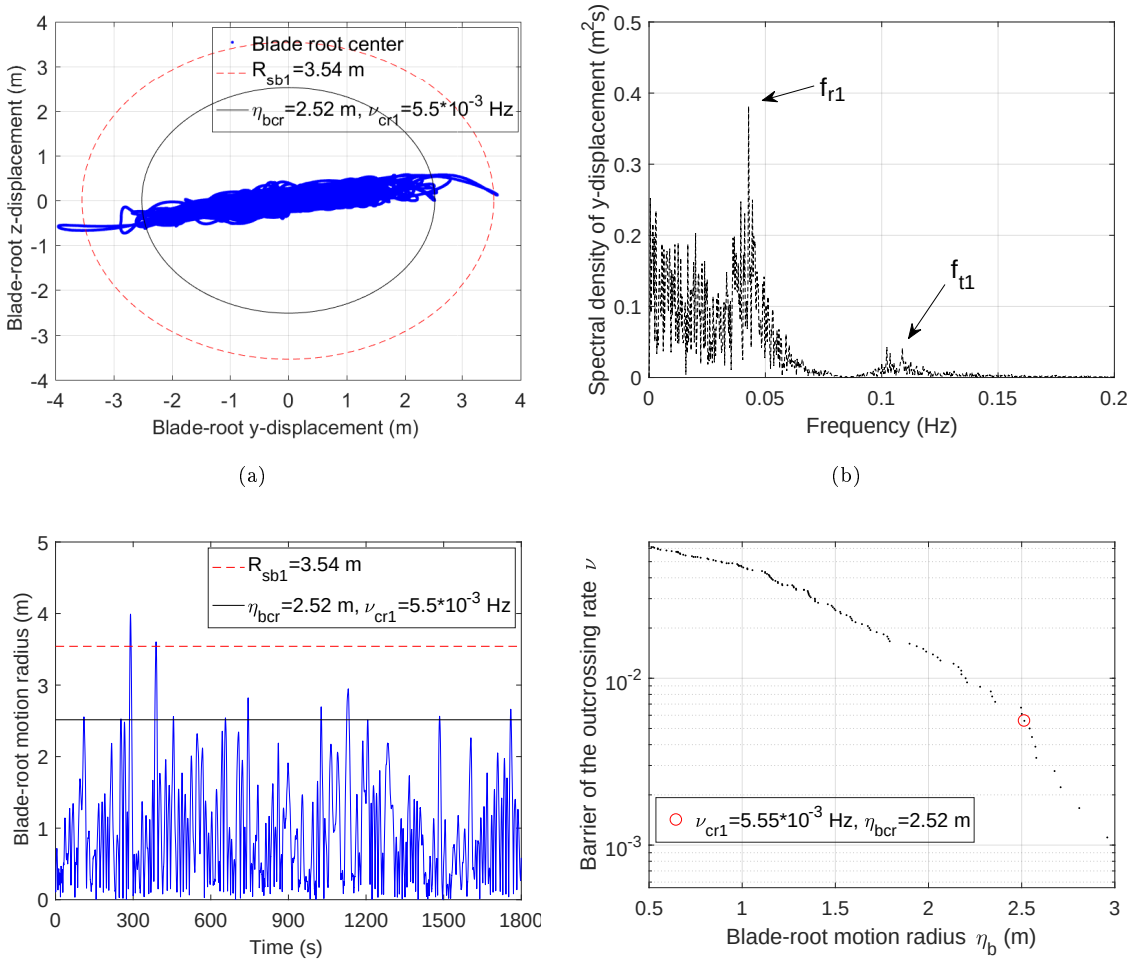

Figure 9: EC10, U_w=10 m/s, TI=0.12, β_{wave}=0 deg, De=25 m, Seed 1: (a) Track of the blade-root center relative to the mean position (b) Response spectrum of the blade-root y-displacement (1800-s) (c) Time history of the blade-root radius relative to the mean position (d) Variation in the outcrossing rate ν with the blade-root motion radius η_b

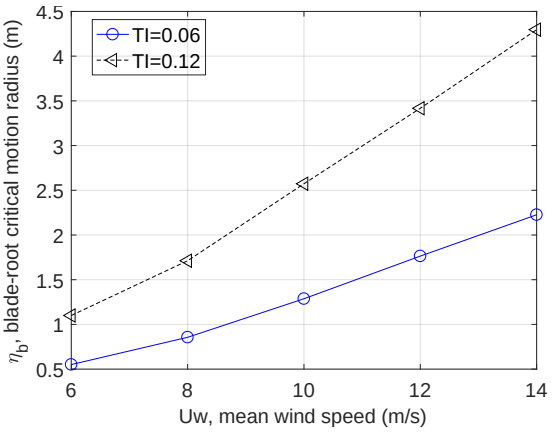

Figure 10: Variation in the derived blade-root critical motion radius η_b with mean wind speed U_w

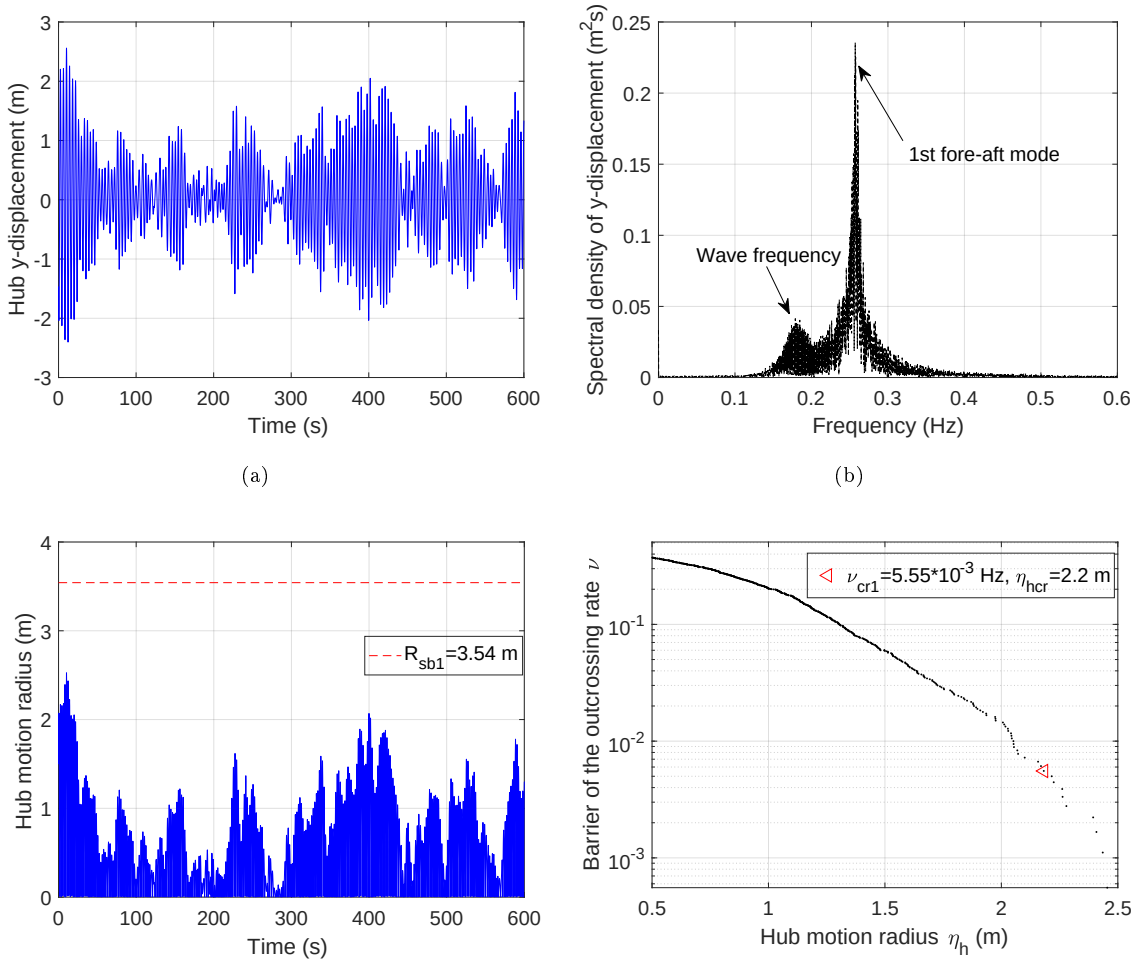

Figure 11: EC5, TI=0.06, H_s=3.28 m, T_p=5.61 s, β_{wave}=0 deg, De=40 m, Seed 1 (a) Hub displacement in the y-direction (600-s) (b) Response spectrum of the hub y-displacement (1800-s) (c) Motion radius of the hub center, (600-s) (d) Variation in the outcrossing rate ν with the hub motion radius η_h (1800-s)

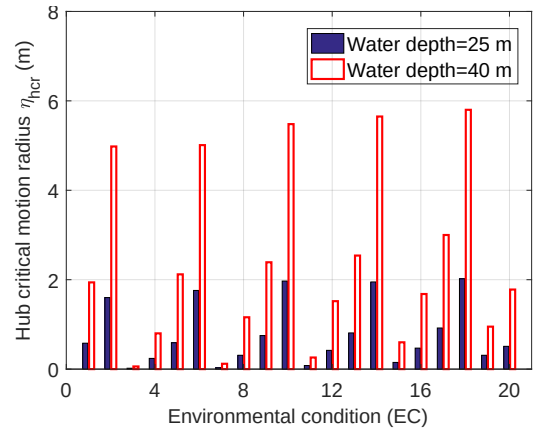

(a)

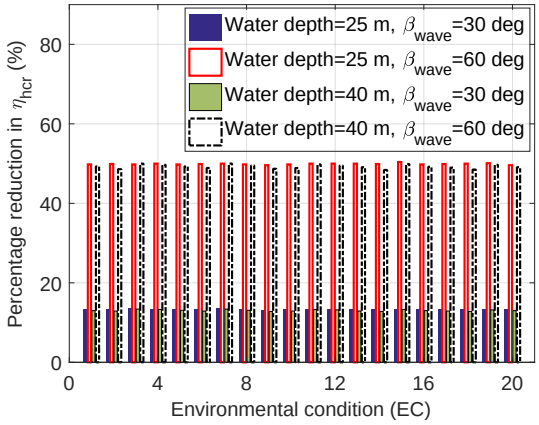

(b)

Figure 12: (a) Comparison of the critical hub motion radius for the two water depths, TI=0.06, β_{wave}=0 deg (b) Percentage reduction in the critical hub motion radius, misaligned waves versus collinear waves (TI=0.06, β_{wave}=0 deg)

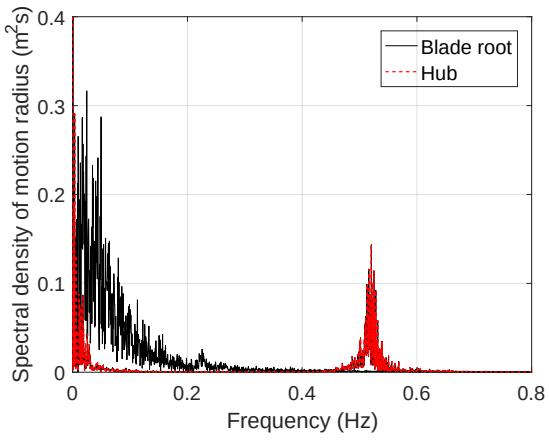

(a)

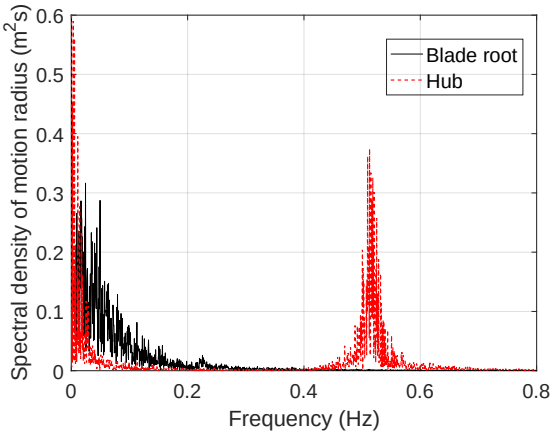

(b)

Figure 13: Response spectra of the motion radius ($\sqrt{y^2+z^2}$), TI=0.12, β_{wave}=0 deg, EC18 (a) De=25 m (b) De=40 m

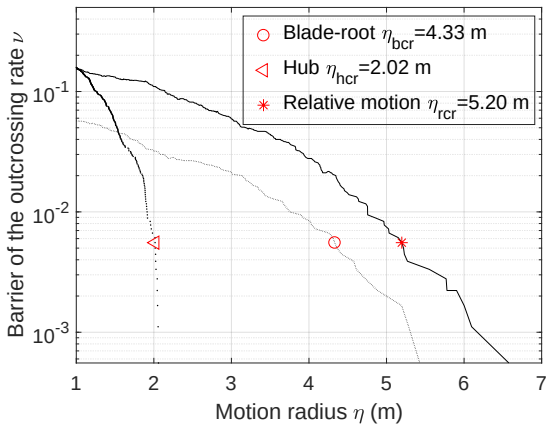

(a)

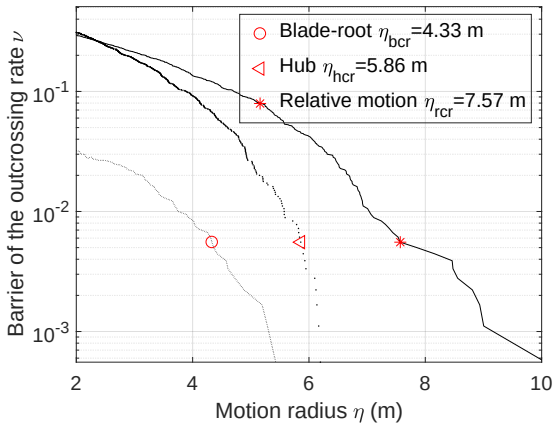

(b)

Figure 14: Variation in the outcrossing rate with motion radius, the red marks corresponding to ν_{cr1} =$5.5{\cdot}10^{-3}$, TI=0.12, β_{wave}=0 deg, EC18 (a) De=25 m (b) De=40 m

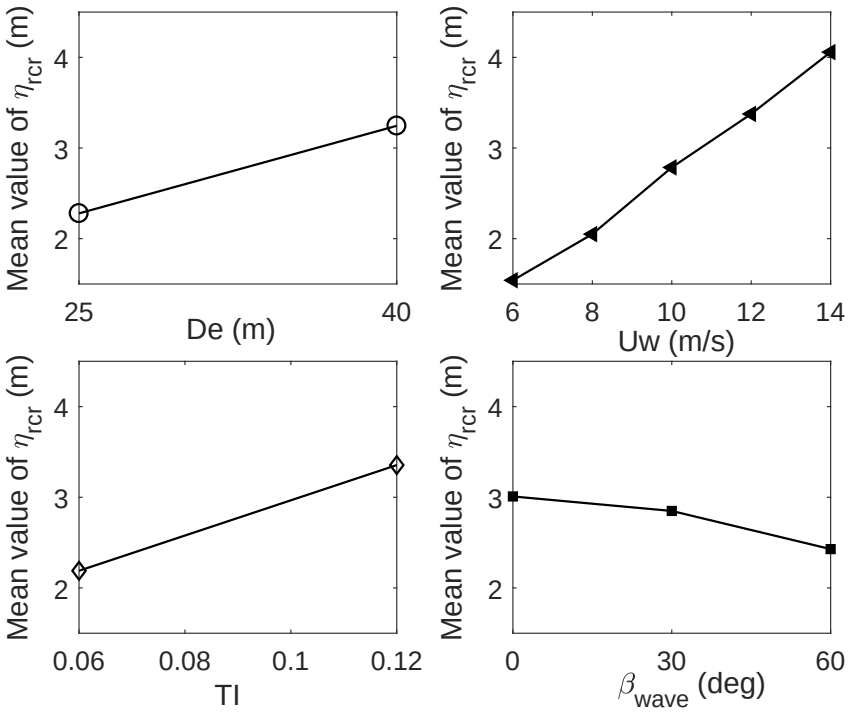

Figure 15: Main effects plot of the relative critical motion radius η_{rcr}

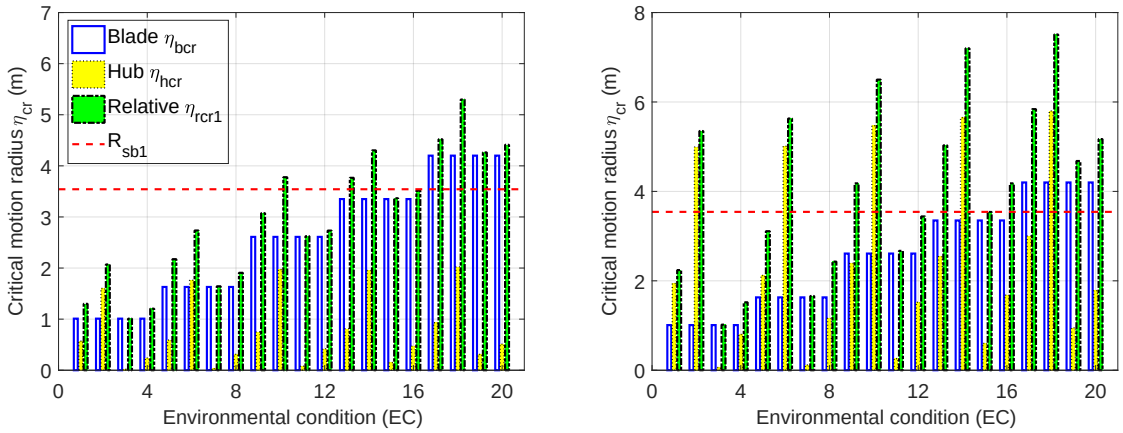

(a)

(b)

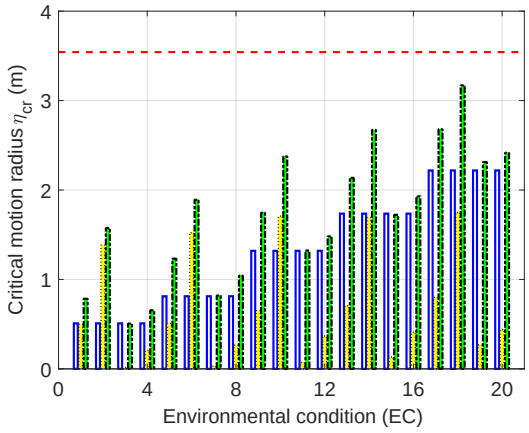

(c)

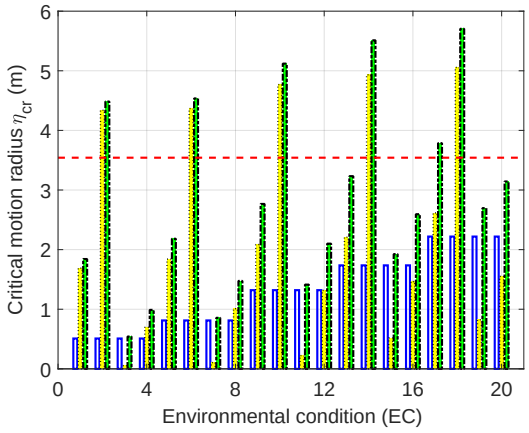

(d)

Figure 16: Comparison of the blade-root, hub, and relative motion radii for selected wind and wave conditions (a) TI=0.12, β_{wave}=0 deg, De=25 m (b) TI=0.12, β_{wave}=0 deg, De=40 m (c) TI=0.06, β_{wave}=30 deg, De=25 m (d) TI=0.06, β_{wave}=30 deg, De=40 m

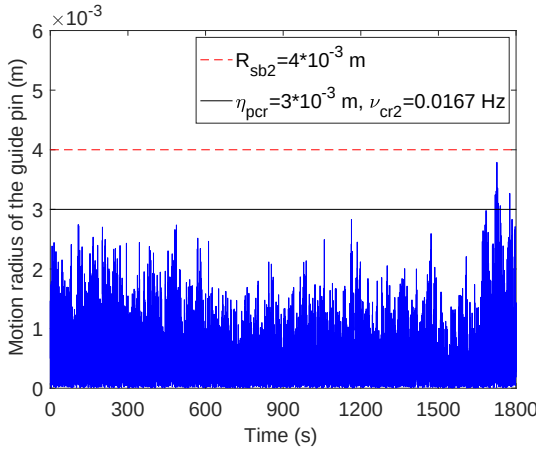

(a)

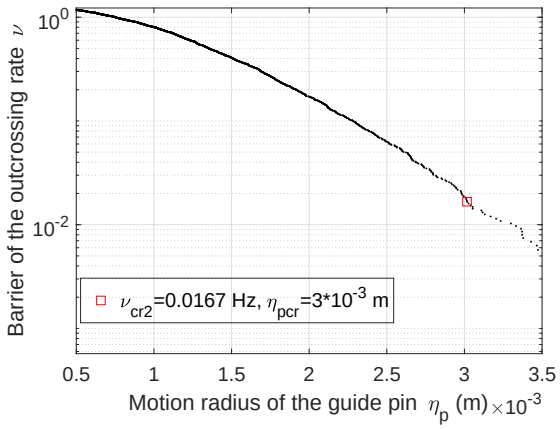

(b)

Figure 17: EC10, U_w=10 m/s, TI=0.12, β_{wave}=0 deg, De=25 m, Seed 1: (a) Time history of the guide pin radius relative to the mean position (d) Variation in the outcrossing rate ν with the guide pin motion radius η_p

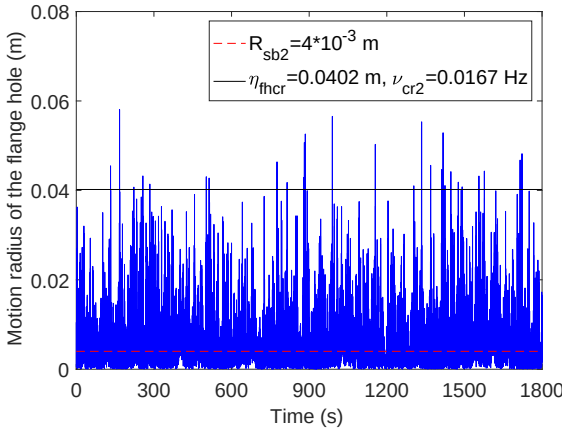

(a)

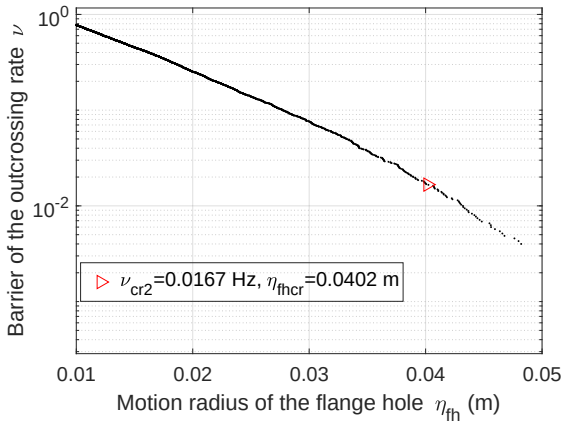

(b)

Figure 18: EC5, U_w=10 m/s, TI=0.06, β_{wave}=0 deg, De=40 m, Seed 1: (a) Time history of the flange hole radius relative to the mean position (d) Variation in the outcrossing rate ν with the flange hole motion radius η_p

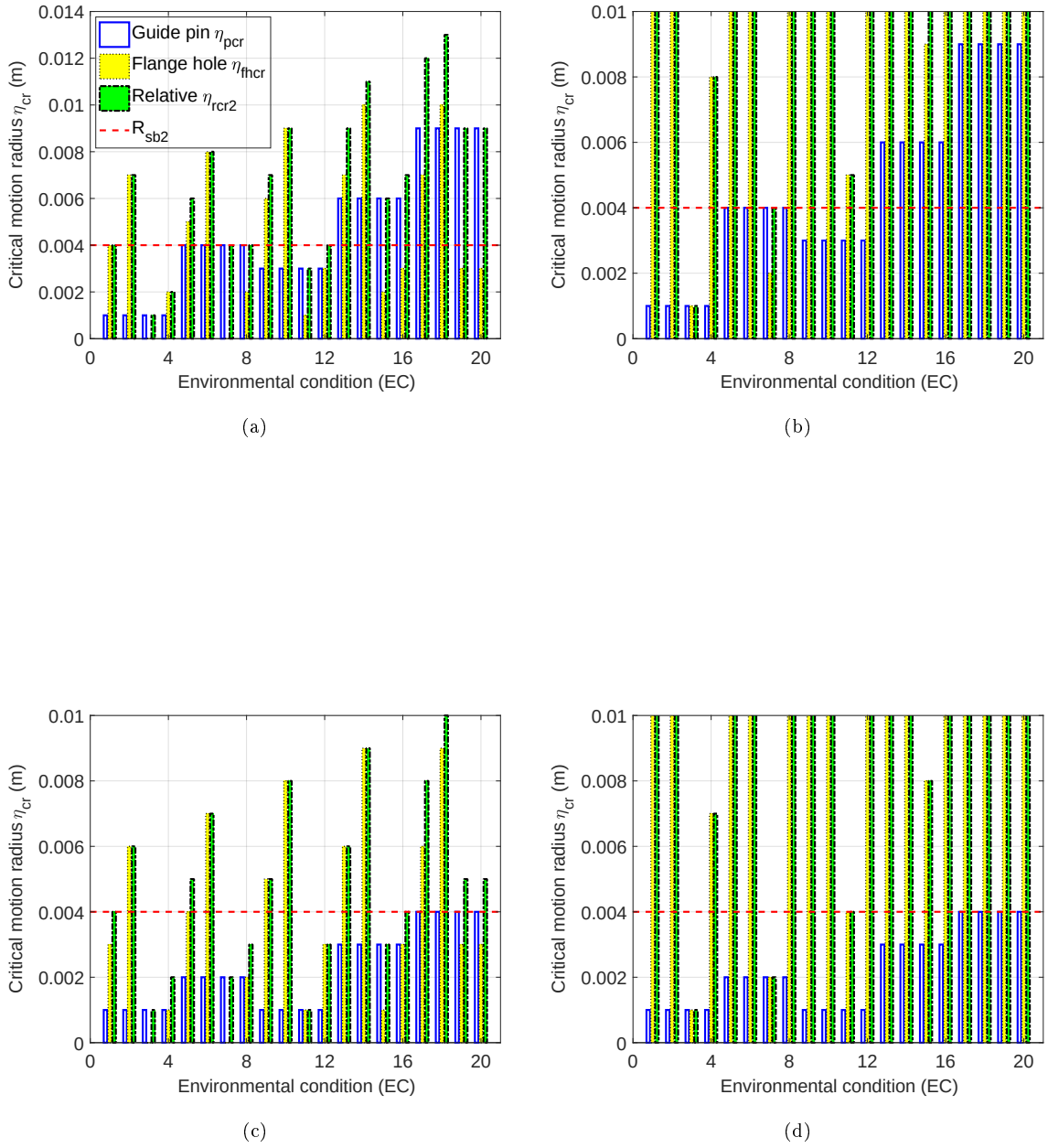

Figure 19: Comparison of the guide-pin, flange-hole, and relative motion radii for selected wind and wave conditions (a) TI=0.12, β_{wave}=0 deg, De=25 m (b) TI=0.12, β_{wave}=0 deg, De=40 m (c) TI=0.06, β_{wave}=30 deg, De=25 m (d) TI=0.06, β_{wave}=30 deg, De=40 m